How precise can atoms of a nanocluster be located in 3D using a tilt series of scanning transmission electron microscopy images?

How precise can atoms of a nanocluster be located in 3D using a tilt series of scanning transmission electron microscopy images?

M. Alania[a], A. De Backer[a], I. Lobato[a], F. F. Krause[b], D. Van Dyck[a], A. Rosenauer[b], S. Van Aert[a,*]

[a] *EMAT, University of Antwerp, Groenenborgerlaan 171, B-2020 Antwerp, Belgium*
[b] *Institüt für Festkörperphysik, Universität Bremen, Otto-Hahn-Alle 1, D-28359 Bremen, Germany*

Abstract

In this paper, we investigate how precise atoms of a small nanocluster can ultimately be located in three dimensions (3D) from a tilt series of images acquired using annular dark field (ADF) scanning transmission electron microscopy (STEM). Therefore, we derive an expression for the statistical precision with which the 3D atomic position coordinates can be estimated in a quantitative analysis. Evaluating this statistical precision as a function of the microscope settings also allows us to derive the optimal experimental design. In this manner, the optimal angular tilt range, required electron dose, optimal detector angles, and number of projection images can be determined.

Keywords: Electron tomography; high-resolution electron microscopy; precision; resolution; Cramér-Rao lower bound

1. Introduction

Nanoclusters play key roles in a wide range of materials and devices because of their unique physical and chemical properties [1]. These properties are determined by the specific three-dimensional (3D) morphology, structure and composition [2]. It is well known that extremely small changes in their local structure may result into significant changes of their properties [3–5]. Therefore, development of techniques to measure the atomic arrangement of individual atoms down to (sub)-picometre precision is important. This allows one to fully understand and greatly enhance the properties of the resulting materials, increasing the number of applications.

Electron tomography using aberration-corrected scanning transmission electron microscopy (STEM) is considered as one of the most promising techniques to achieve atomic resolution in three dimensions. In conventional electron tomography, a series of images is acquired by tilting the sample over a large angular range, with an increment of typically 1 or 2 degrees. After alignment of the projection images, the tilt series is combined into a 3D reconstruction of the original object through a mathematical algorithm [6–8]. High-angle annular dark field (HAADF) STEM [9, 10] has become a popular technique for materials characterisation in 3D because of its so-called Z-contrast. In this imaging mode, the images scale with the atomic number Z and the specimen thickness. For many years, the ultimate goal has been to achieve electron tomography with atomic resolution. Although this is not yet a standard possibility for all structures, significant progress has recently been achieved using different approaches [11–13]. Once the atoms can be resolved in 3D, the next challenge is to refine the atom positions in a quantitative manner [14, 15]. However, the answer to the question how precise these measurements are, is still open. Ultimately, a precision in the (sub)-picometre range is desired. The subject of this paper is to investigate if this goal is within reach.

In this paper, we investigate the theoretical limits with which atoms of a nanocluster can be located in 3D based on the acquisition of a tilt series of ADF STEM images. Ultimately, the reliability with which one can measure the atom positions is limited by the unavoidable presence of electron counting noise in the acquired projection images, which is the so-called Poisson noise or shot noise. This sets fundamental limits to the precision that can be obtained. Use of the concept of Fisher information allows us to determine an expression for the highest attainable precision with which positions of atoms can be located in 3D, or equivalently, an expression for the lower bound on the attainable variance. It is essential to remark that this lower bound is independent of the estimation method used. In this context this means that the CRLB is independent of the tomographic reconstruction algorithm. The expression for the lower bound on the variance not only helps to compute the precision that can ultimately be achieved but also to determine the optimal angular tilt range, required electron dose, optimal detector angles, and number of projection images. Since we are interested in the theoretical limits, we assume an ideal experimental setup for the computation of the ultimate precision. This means that we assume that scan noise and alignment errors can be avoided or can be corrected for [16–18] and that the sample is a perfect free-standing nanocluster. Therefore, beam damage, the re-arrangement of the nanocluster, and the effect of a sample support for the nanocluster are not considered in this theoretical study.

Furthermore, it is important to note that this concept of precision is different from the well-known concept of resolution,

*Corresponding author. Tel:+32-32653252; fax:+32-32653318
Email address: sandra.vanaert@uantwerpen.be (S. Van Aert)

expressing the possibility of perceiving separately two point sources. Resolution is interpreted in many ways since it is not unambiguously defined. Therefore, several resolution criteria, including Rayleigh's [19] have been proposed in the past. Such classical resolution criteria are concerned with calculated images, that is, noise-free images exactly described by a known parametrised model. However, these criteria do not take the signal-to-noise ratio into account and disregard the possibility of using this prior knowledge about the image intensity distribution to extract numerical results from the observations by model fitting using parameter estimation methods. For experimentally acquired images, model fitting never results in a perfect match in the presence of noise such that the component locations can only be estimated with limited statistical precision [20, 21]. This statistical precision will be quantified in this paper for the coordinates of the central atom of a nanocluster.

This paper is organised as follows. In section 2, the parametric models for the intensity observations are described. In section 3, an expression is derived for the attainable precision with which atoms can be located in 3D. Section 4 describes how images of gold nanoclusters have been simulated and the approximations that have been made. In section 5, the dependence of the attainable precision on the choice of experimental settings is studied. In section 6, conclusions are drawn.

2. Parametric model for the intensity observations

A parametric model, describing the expectations of the intensities observed when recording a tilt series of ADF STEM images, is needed in order to derive an expression for the attainable precision. In this section, such a model will be derived using both the multislice method and the Gaussian approximation model proposed by Curley et al. [22]. Although the multislice method is more accurate to describe the electron-object interaction, it is very time-consuming, especially when simulating a tilt series of images. Therefore, the Gaussian approximation model will be used as well in order to perform fast, albeit approximate, simulations that will allow us to get insight into the precision that can be attained to locate atoms in three dimensions.

2.1. Rotation of a nanocluster

A tilt series of ADF STEM images of a nanocluster needs to be modelled, where the positions of the N atoms correspond to the elements of the parameter vector $\beta = (\beta_{x1}, \beta_{y1}, \beta_{z1}, \ldots, \beta_{xN}, \beta_{yN}, \beta_{zN})$. In the reference coordinate system, we assume that the origin is located at the position of the central atom of the nanocluster. In this paper, single-axis tomography is assumed in which two-dimensional images are obtained when tilting a nanocluster around a fixed tilt axis. The tilt axis corresponds to the y-axis and the electron beam is assumed to be parallel to the z-axis as indicated in Fig. 1. For a rotation over $[-90, 90]$ degrees, the x- and z-axis become equivalent for a symmetric structure around the rotation axis y. Furthermore, the tilt angles θ^j, $j = 1, \ldots, J$ are equidistantly sampled in the interval $[-\alpha, +\alpha]$ corresponding to a full angular tilt range if $\alpha = \pi/2$. At each tilt angle θ^j, the locations of the N atoms $\beta^j = (\beta^j_{x1}, \beta^j_{y1}, \beta^j_{z1}, \ldots, \beta^j_{xN}, \beta^j_{yN}, \beta^j_{zN})$ with respect to the reference coordinates system are then given by:

$$\begin{bmatrix} \beta^j_{xi} \\ \beta^j_{yi} \\ \beta^j_{zi} \end{bmatrix} = \begin{bmatrix} cos\theta^j & 0 & sin\theta^j \\ 0 & 1 & 0 \\ cos\theta^j & 0 & -sin\theta^j \end{bmatrix} \begin{bmatrix} \beta_{xi} \\ \beta_{yi} \\ \beta_{zi} \end{bmatrix} \quad (1)$$

In the following subsections, the Gaussian approximation model and the multislice method will be used in order to simulate images for each tilt angle θ^j.

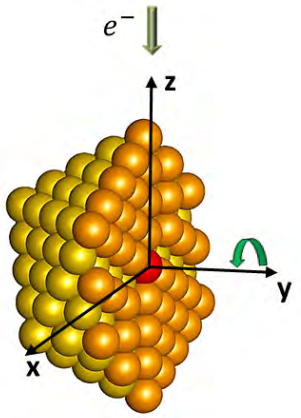

Figure 1: Cross-section of a nanocluster indicating the x-, y- and z-axis, the central atom (red atom), and the atoms of the central plane (orange atoms).

2.2. The multislice method

The multislice method is known as an accurate manner to model the quantum mechanical electron-object interaction [23–26]. Its aim is to describe the electron wave function by solving the high energy Schrödinger equation. Therefore, the sample potential is divided into many slices perpendicular to the electron beam. Each slice is chosen thin enough such that it can be considered as a phase object, which only modifies the phase of the incident wave. The potential between consecutive slices is considered to be zero and the propagation of the electron wave within the slice is approximated by the Fresnel propagator. By repeated application of the phase object transmission and vacuum propagation, the electron wave can be calculated at any depth. Especially when simulating ADF STEM images, not only dynamical scattering but also thermal diffuse scattering needs to be taken into account. Indeed, electrons scattered toward the ADF detector, may also have undergone a phonon scattering event. An efficient multislice formulation that does include phonon scattering is the frozen phonon method [27], in which multiple multislice calculations are performed for different thermal displacements of the atoms. The resultant intensity in the detector plane is then averaged over the different configurations. The frozen phonon method is known as the most complete method for the computation of ADF STEM images. However, modelling an ADF STEM image is computationally very expensive. Indeed, the intensity in the detector plane must

be summed over the detector geometry, and this calculation repeated for all probe positions $\mathbf{r_0} = (x_k, y_l)$ in the image. To simplify these calculations to some extent, the absorptive potential multislice method has been suggested by Allen et al. [28] and Ishizuka [24]. In this method, an imaginary term in the atomic potential is included to account for absorption. It has been shown that for nanoparticle systems and thin layered specimens, the absorptive potential multislice method agrees with full frozen phonon calculations [29, 30].

In this paper, absorptive potential multislice calculations have been carried out with the STEMsim program [31] expressing simulated images as a fraction f_{kl}^j of electrons recorded by the detector ($f_{kl}^j < 1$). The indices (k, l) and j correspond to the probe located at the position (x_k, y_l) and tilt angle θ^j, respectively. In these simulations, the finite size of the source is taken into account by a two-dimensional convolution with the intensity distribution of the source image, which can be modelled as a Gaussian distribution [32].

2.3. The Gaussian approximation model

The Gaussian approximation model is based on the assumption of kinematic scattering of electrons and has been proposed by Curley et al. for monometallic systems [22]. In this model, the ADF STEM image intensity of a nanocluster is described as a linear combination of image contributions of all atoms constituting the object under study. When assuming a three-dimensional Gaussian function for each atom, the contribution of atom i to a projection image is given by [33]:

$$\left(f_{kl}^j\right)^i = Z_i^\zeta \exp\left(-\gamma \frac{(x_k - \beta_{xi}^j)^2 + (y_l - \beta_{yi}^j)^2}{r_i^2}\right) \quad (2)$$

where (x_k, y_l) is the position of the probe and $(\beta_{xi}^j, \beta_{yi}^j)$ is the position of the ith atom in projection at tilt angle θ^j. Furthermore, γ is an atom type dependent constant, determining the decay of the electron scattering as a function of the distance to the centre of the projected atom, Z_i and r_i are the atomic number and atomic radius of the ith atom, respectively, and ζ is a scattering constant depending on the collection angle of the detector. Realistic values for the parameters ζ and γ can be obtained by fitting the model given by Eq. (2) to an image of a single atom obtained by averaging and rescaling multislice simulations for an appropriate range of thicknesses. For all atoms N of the nanocluster contributing to the image, the intensity at the pixel (x_k, y_l) at tilt angle θ^j is then given by:

$$f_{kl}^j = \sum_{i=1}^{N} \left(f_{kl}^j\right)^i \quad (3)$$

2.4. The image recording

In ADF STEM imaging, a focused electron probe is scanned across the sample in a raster fashion and the transmitted electrons are collected by an annular detector placed in the back focal plane. The image is thus recorded as a function of the probe position (x_k, y_l). Therefore, the position of the probe directly corresponds to an image pixel at the same position. The recording device consists of $K \times L$ equidistant pixels of area $\Delta x \times \Delta y$, where Δx and Δy are the probe sampling distances in the x- and y-direction, respectively. Pixel (k, l) corresponds to position $(x_k, y_l) \equiv (x_1 + (k-1)\Delta x, y_1 + (l-1)\Delta y)$ with $k = 1, \ldots, K$ and $l = 1, \ldots, L$ and (x_1, y_1) represent the position of the pixel in the bottom left corner of the field of view.

The number of incident electrons per probe position N_e is given by the following expression:

$$N_e = \frac{I\tau}{e} \quad (4)$$

with I the probe current in ampere, τ the recording dwell time for one pixel, and $e = 1.6 \times 10^{-19}$ C the electron charge. The expected number of detected electrons per pixel position (k, l) at tilt angle θ^j equals

$$\lambda_{kl}^j = f_{kl}^j \frac{I\tau}{e} \quad (5)$$

with f_{kl}^j the fraction of electrons expected to be recorded by the detector [34].

3. Statistical measurement precision

In the preceding section, parametric models for the intensity observations made at three-dimensional nanoclusters were derived. These models describe the expected number of electrons arriving at the STEM detector and are parametric in the locations β of all atoms constituting a nanocluster. In what follows, it will be shown how these location parameters enter the probability density function of the statistical observations. From this parametrised probability density function, the so-called Cramér-Rao Lower Bound (CRLB) may be computed [35, 36], which is a lower bound on the variance of the parameters. It is important to notice that this lower bound is independent of the estimation method used, i.e. independent of the tomographic reconstruction algorithm. For the purpose of this paper, the most important parameters are the three-dimensional positions of the atoms in a nanocluster. Therefore, an expression for the CRLB on the variance of the positions will be derived in subsection 3.2 based on the joint probability density function of the observations, which will be derived in subsection 3.1.

3.1. The joint probability density function of the observations

In any STEM experiment, sets of observations made under the same conditions differ from experiment to experiment. These fluctuations have to be specified, which is the subject of this section. The usual way to describe this behaviour is to model the observations as stochastic variables. Stochastic variables are defined by probability density functions [36]. In a STEM experiment the observations are electron counting results. The fluctuations of these observations are denoted as electron counting noise, Poisson noise, or shot noise. The corresponding probability density function can be modelled as a Poisson distribution.

Consider a set of stochastic observations w_{kl}^j, $k = 1,\ldots,K$, $l = 1,\ldots,L$, and $j = 1,\ldots,J$. Then the vector w defined as

$$w = (w_{11}^1,\ldots,w_{KL}^J)^T \tag{6}$$

represents the column vector of these observations of dimension $K \times L \times J$, where $K \times L$ corresponds to the dimension of each projection image and J corresponds to the number of images in the tilt series. The observations are assumed to be statistically independent and have a Poisson distribution. Therefore, the probability that the observation w_{kl}^j is equal to ω_{kl}^j is given by [37]

$$\frac{\left(\lambda_{kl}^j\right)^{\omega_{kl}^j}}{\omega_{kl}^j!}\exp\left(-\lambda_{kl}^j\right) \tag{7}$$

with λ_{kl}^j the expected number of detected electrons at pixel (k,l) at tilt angle θ^j for which an expression is given by Eq. (5). Since the observations are assumed to be statistically independent, the probability $P(\omega,\beta)$ that a set of observations is equal to $\omega = (\omega_{11}^1,\ldots,\omega_{KL}^J)^T$ is the product of all the probabilities described by Eq. 7:

$$P(\omega,\beta) = \prod_{j=1}^{J}\prod_{k=1}^{K}\prod_{l=1}^{L}\frac{\left(\lambda_{kl}^j\right)^{\omega_{kl}^j}}{\omega_{kl}^j!}\exp\left(-\lambda_{kl}^j\right) \tag{8}$$

This function is called the joint probability density function of the observations. Note that the location parameters β enter $P(\omega;\beta)$ via the expression λ_{kl}^j, given by Eq. (5). Indeed, from section 2, it follows that in order to compute the expected number of detected electrons, use is made of absorptive potential multislice calculations or the Gaussian approximation model, which both require the positions of all atoms present in the nanocluster as an input. In the following subsection, it will be shown how this expression for the joint probability density function can be used in order to compute the CRLB.

3.2. The Cramér-Rao Lower Bound CRLB

In this subsection, the CRLB is discussed, which is a theoretical lower bound on the variance of any unbiased estimator. Therefore, this expression can be used in order to determine the attainable precision with which the location parameters of all atoms present in a nanocluster can be estimated. Suppose that an experimenter wants to measure the position parameters $\beta = (\beta_{x1},\beta_{y1},\beta_{z1},\ldots,\beta_{xN},\beta_{yN},\beta_{zN})$ of a set of N atoms of a nanocluster in a quantitative manner from a set of projection images acquired using a tomography experiment. For this purpose, one can use many estimators. An estimator is a function of the observations that is used to compute the parameters. In this context, an estimator can be a tomographic reconstruction algorithm. The precision of an estimator is represented by the variance or by its square root, the standard deviation. Generally, different estimators will have different precisions. It can be shown, however, that the variance of unbiased estimators will never be lower than the CRLB, which is independent of the used estimation method. Fortunately, there exists a class of estimators (including the maximum likelihood estimator) that achieves this bound at least asymptomatically, that is, for the number of observations going to infinity. For details of this lower bound we refer to [35, 36].

The CRLB follows from the concept of the Fisher information. The Fisher information matrix F for estimation of the position parameters of a set of N atoms $\beta = (\beta_{x1},\beta_{y1},\beta_{z1},\ldots,\beta_{xN},\beta_{yN},\beta_{zN})$ is defined as

$$F = -E\left[\frac{\partial^2 \ln P(\omega;\beta)}{\partial\beta\partial\beta^T}\right] \tag{9}$$

where $P(\omega;\beta)$ is the joint probability density function of the observations given by Eq. (8) and

$$\frac{\partial^2 \ln P(\omega;\beta)}{\partial\beta\partial\beta^T} \tag{10}$$

is the $3N\times3N$ Hessian matrix of $\ln P(\omega;\beta)$ of which the $(p,q)th$ element is defined as:

$$\frac{\partial^2 lnP(\omega;\beta)}{\partial\beta_p\partial\beta_q} \tag{11}$$

where β_p and β_q correspond to the p and qth element of the vector β, respectively.

Suppose that $\hat{\beta} = (\hat{\beta}_{x1},\hat{\beta}_{y1},\hat{\beta}_{z1},\ldots,\hat{\beta}_{xN},\hat{\beta}_{yN},\hat{\beta}_{zN})^T$ is an unbiased estimator of β. The Cramér-Rao inequality then states that [38]

$$\mathrm{cov}(\hat{\beta},\hat{\beta}) \geq F^{-1} \tag{12}$$

where $\mathrm{cov}(\hat{\beta},\hat{\beta})$ is the $3N \times 3N$ variance-covariance matrix of the estimator $\hat{\beta}$, defined by its $(p,q)th$ element $\mathrm{cov}(\hat{\beta}_p,\hat{\beta}_q)$. Its diagonal elements are thus the variances of the elements of $\hat{\beta}$. The matrix F^{-1} is called the Cramér-Rao lower bound on the variance of $\hat{\beta}$. The Cramér-Rao inequality (12) expresses that the difference between the left-hand and right-hand member is positive semi-definite. A property of a positive semi-definite matrix is that its diagonal elements cannot be negative. This means that the diagonal elements of $\mathrm{cov}(\hat{\beta},\hat{\beta})$ will always be larger than or equal to the corresponding diagonal elements of the inverse of the Fisher information matrix. Therefore, the diagonal elements of F^{-1} define lower bounds on the variances of the elements of $\hat{\beta}$

$$\mathrm{var}(\hat{\beta_p}) \geq F^{-1}(p,p) \tag{13}$$

where $p = 1,\ldots,3N$ and $F^{-1}(p,p)$ is the (p,p)th element of the inverse of the Fisher information matrix. The elements $F(p,q)$ may be calculated explicitly using Eqs. (5)-(11) [34]:

$$F(p,q) = \sum_{j=1}^{J}\sum_{k=1}^{K}\sum_{l=1}^{L}\frac{1}{\lambda_{kl}^j}\frac{\partial\lambda_{kl}^j}{\partial\beta_p}\frac{\partial\lambda_{kl}^j}{\partial\beta_q}. \tag{14}$$

Eq. (14) is derived from the definition of the Fisher information given by Eq. (9) using the knowledge of the joint probability density function of the observations. This joint probability density function and the expectation values of the observations are the only requirements to be able to compute the ultimate precision for locating the atoms in 3D. The derivative of λ_{kl}^j with

respect to $\hat{\beta}$ in Eq. (14) may be calculated from the parametric model of the intensity observations described in section 2. For the multislice method, this derivative needs to be computed numerically, as will be discussed in more detail in subsection 5.1. Unlike the multislice method, the derivatives can be calculated analytically for the Gaussian approximation model leading to a rule of thumb. Following the approach of [34], it can be demonstrated using Eqs. (1), (2), and (14) that the attainable precision of the x-, y-, and z-coordinate of a single atom modelled as a Gaussian function equals:

$$\sigma_x^2 = \sigma_z^2 \approx \frac{r^2}{\gamma N_p}$$
$$\sigma_y^2 \approx \frac{r^2}{2\gamma N_p} \qquad (15)$$

where $\left(\frac{r^2}{2\gamma}\right)^{1/2}$ corresponds to the Gaussian width, r equals the atomic radius, γ is a constant dependent on the atom type, and N_p is the total electron dose. This total electron dose equals:

$$N_p = \pi J \frac{Z^\zeta r^2}{\gamma \Delta x \Delta y}$$

where J denotes the number of projections, Z the atomic number, ζ a scattering constant depending on the collection angle of the detector, and Δx and Δy the pixel size in x- and y-direction. For larger clusters, the precision σ of the x-, y-, and z-coordinate can be described by the sum of the precision for one atom given by Eq. (15) and a power law describing the dependence on the cluster diameter.

4. Simulation settings

Simulations for four gold nanoclusters of different sizes have been performed as illustrated in Fig. 2. The bulk structure of gold is an FCC structure. However, for small nanoclusters, the atomic structure deviates from this ideal FCC lattice. In this paper, nanoclusters with a Mackay icosahedral morphology have been considered [39]. The interatomic distance in these nanoclusters equals 3.0 Å. As discussed in section 2, both the multislice method and a Gaussian approximation model have been used to simulate tilt series of images. The expression of the Gaussian approximation model is given by Eq. (3), where an expression for the fractional intensities f_{kl}^j of single atoms is given by Eq. (2). Numbers for the parameters ζ and γ are obtained by fitting this expression to an image of a single atom inferred from averaging and rescaling the multislice simulated images of the central column of the four clusters along the [001] zone axis. Use has been made of the STEMsim program [31] to perform multislice calculations under the absorptive potential approximation. Furthermore, the finite source size is modelled by convolving the resulting image with a Gaussian distribution. In Appendix A, it is demonstrated that this is a good approximation for the computation of the precision of the central atom of a nanocluster. The settings used for the multislice simulations are summarised in Table 1; for the spherical aberration and defocus the Scherzer settings have been chosen [40, 41]. Furthermore, it is shown in Appendix B that it is suitable to use the same value for the Debye-Waller factor of all the atoms in the nanocluster when computing the precision of the central atom.

Table 1: Overview of simulation settings.

Slice thickness	2.0 Å
Debye-Waller factor	0.63 Å^2
Acceleration voltage	300 kV
Defocus	-88.74 Å
Spherical aberration	0.04 mm
Convergence angle	21.06 mrad
FWHM of the source image	0.7 Å
Pixel size in the STEM image	0.15 Å
Pixel size of the numerical grid	0.032 Å
Beam current	10 pA
Dwell time	2 μs
Incident electron dose per image	5555 e$^-$/Å^2

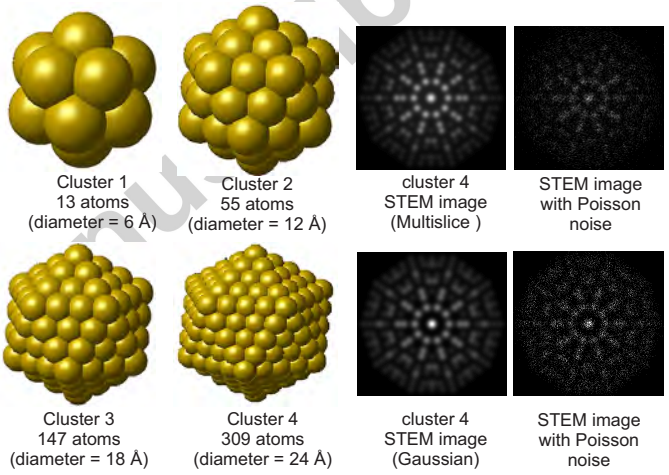

Figure 2: The four smallest gold nanoclusters with icosahedral structure and a comparison between the Gaussian model and multislice simulation without and with Poisson noise.

For each simulated image of the electron tomography tilt series, a super cell is created of which the dimension in the x- and y-direction equals the diameter of the nanocluster under consideration plus 10 Å extra to avoid wrapping around effects. The dimension in the z-direction equals the diameter of the cluster.

5. Results and discussion

5.1. Calculation of the attainable precision

In this subsection, we will discuss and describe the steps followed in order to quantify the attainable precision of the 3D atomic position coordinates of the central atom inside a gold nanocluster. The attainable precision, i.e. the lower bound on the standard deviation σ, is given by the diagonal elements of the inverse Fisher information matrix F, given by Eq. (14). From this expression, it is clear that the elements of the Fisher information matrix have to be calculated by using the derivatives of the parametric model for the intensity observations λ

with respect to the 3D atomic coordinates. The parametric models for the intensity observations λ are given by the simulated 2D projection images using either the Gaussian approximation model or multislice simulations. For the Gaussian approximation model, these derivatives can be calculated analytically, since this model is parametric in the atomic coordinates. However, for the multislice simulations, the derivatives cannot be calculated analytically, since the simulation results from a numerical solution of the high energy Schrödinger equation. In order to calculate the partial derivatives for the multislice method, an additional set of multislice simulations is required in which a single atom of the nanocluster is shifted along an axis. For example, for the derivatives of the central atom with respect to the x-coordinate, the central atom of the nanocluster is displaced along the x-axis. The partial derivatives are then approximated using the finite difference quotient:

$$\lambda'(x) \approx \frac{\lambda(x) - \lambda(x-h)}{h} \tag{16}$$

where h denotes the shift of the atom. Similarly, the derivatives with respect to the y- and z-axis, for the other atoms, and for the different projected images of the tilt series can be calculated. The calculation of all the derivatives for a nanocluster of N atoms for J tilt angles thus requires $J(3N+1)$ simulations. In order to test if the number of simulations needed for the calculation of the Fisher information matrix can be reduced, the Gaussian approximation model will be used. This will be discussed in subsection 5.2. Furthermore, the optimal tilt range and the optimal number of projections will be evaluated for the Gaussian approximation model in subsections 5.3 and 5.4. Next, in subsections 5.5 and 5.6, multislice simulations will be used in order to determine the optimal detector angles of the annular STEM detector and the attainable precision for locating the central atom of the four nanoclusters. Finally, in subsection 5.7, the method is applied for the determination of the minimally required electron dose in order to attain a pre-specified precision to locate the atoms in 3D.

5.2. Determination of the number of simulations for the computation of the attainable precision

In this subsection, the attainable precision for locating a nanocluster in 3D is evaluated as a function of the number of parameters that is included in the calculation of the Fisher information matrix. From Eq. (14), it can be seen that the calculation of the Fisher information matrix requires the derivatives of the expectation model λ_{kl}^{j} with respect to all the position coordinates of the atoms of the nanocluster, i.e. $\beta = (\beta_{x1}, \beta_{y1}, \beta_{z1}, \ldots, \beta_{xN}, \beta_{yN}, \beta_{zN})$, $3N$ parameters where N denotes the number of atoms in the cluster. Here, we investigate if the attainable precision is affected when the number of parameters is reduced. It is important to note that the inverse of the Fisher information matrix does not equal the inverse of the elements of the Fisher information matrix, especially in the presence of significant correlations between the parameters. This means that the attainable precision of e.g. the central atom is influenced by the presence of neighbouring atoms. In practice, this means that e.g. the precision of the central atom will be lower when the exact location of the other atoms is unknown and should be estimated simultaneously. In order to investigate the importance of the number of parameters for the attainable precision for locating the central atom of a nanocluster, the attainable precision will be computed using three different approaches:

1. using all the atoms: the derivatives with respect to all the position coordinates as described by Eq. (14) are calculated,
2. using the atoms of the central plane (orange atoms in Fig. 1): the derivatives with respect to the position coordinates of the atoms of the central plane, i.e. parallel to the incident beam and perpendicular to the rotation axis, are calculated,
3. using the central atom only (red atom in Fig. 1): the derivatives with respect to the x-, y-, and z-coordinate of the central atom are computed.

The CRLB has been computed for these three different approaches using the Gaussian approximation model for 31 projection images over a tilt range of $[-90, 90]$ degrees. An incident electron dose of 5555 $e^-/\text{Å}^2$ per image will be used, which corresponds to a beam current of 10 pA, a pixel dwell time of 2 μs, and a pixel size of 0.15 Å. The results for the precision are shown in Fig. 3 as a function of the cluster diameter. Note that the values for the precision for 1 atom (cluster diameter equal to 0) in this figure can be approximated by the rule of thumb given by Eq. (15) and that the precision as a function of the cluster diameter can be approximated by the sum of the precision for one atom given by Eq. (15) and a power law. From this figure, it can be seen that the precision is not significantly affected when reducing the number of parameters for the calculation of the Fisher information matrix. Therefore, it is allowed to use only the central atom, i.e. the derivatives with respect to the position coordinates of the central atom, in order to evaluate the attainable precision. Throughout the rest of this paper, the precision will therefore be calculated using the derivatives with respect to the position coordinates of the central atom only. This means that the number of simulations needed for the numerical approximation of the derivatives of the Fisher information matrix when computing the precision for the accurate multislice simulations can be reduced drastically from $J(3N+1)$ to $4J$.

5.3. The optimal angular tilt range

In this subsection, the lower bound on the standard deviation for locating the central atom of a nanocluster in 3D is evaluated for different tilt ranges for a fixed number of projection images, such that the total electron dose is kept constant. Due to the rotation of the nanocluster, the precision with which the atoms can be located in the z-direction will improve. Therefore, it is important to evaluate the attainable precision as a function of the tilt range of the nanocluster. In Fig. 4, the precision σ of the x-, y-, and z-coordinate for locating the central atom is shown as a function of the angular tilt range for a fixed number of 31

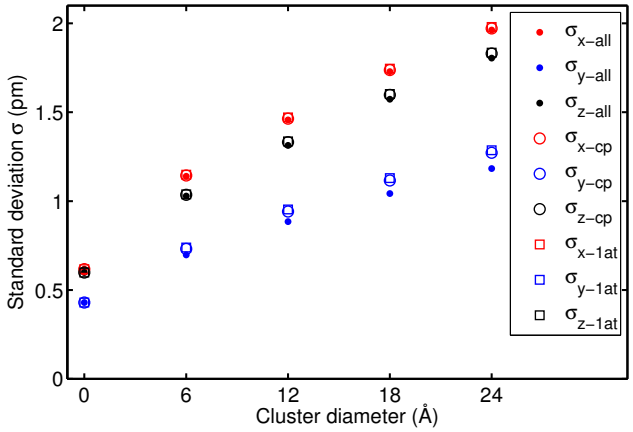

Figure 3: The precision σ of the x-, y-, and z-coordinate for locating the central atom in a nanocluster as a function of the cluster diameter using all the atoms (all), the atoms of the central plane (cp), or the central atom only (1at) based on simulations using the Gaussian approximation model for 31 projection images over a tilt range of $[-90, 90]$ degrees, and an electron dose of 5555 $e^-/\text{Å}^2$ per image.

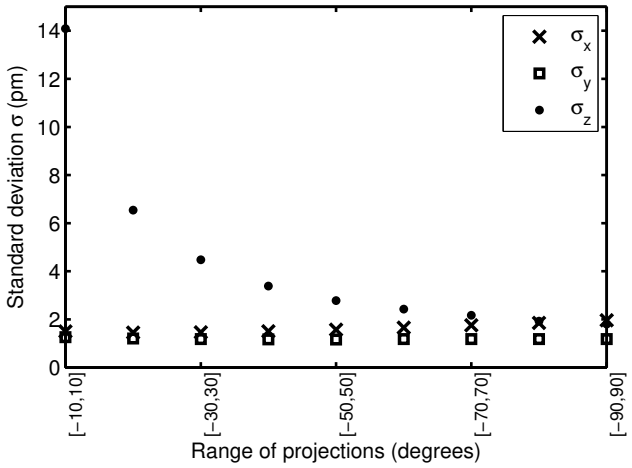

Figure 4: The precision σ of the x-, y-, and z-coordinate as a function of the angular tilt range for locating the central atom of a nanocluster with 309 atoms based on simulations using the Gaussian approximation model using a fixed number of 31 projection images for an incident electron dose of 5555 $e^-/\text{Å}^2$ per image.

projection images and an incident electron dose of 5555 $e^-/\text{Å}^2$ per image. From this figure, we can see the precision for locating the atoms in the z-direction improves significantly when increasing the angular tilt range. As expected, the precision for locating the atoms in the y-direction does not change significantly when increasing the angular tilt range, since it mainly depends on the number of projection images in the tilt series. For the precision for locating the atoms in the x-direction, a small increase in precision is observed when increasing the tilt range. This can be derived from the fact that when rotating the cluster around the y-axis, information on the z-coordinate will be gained, but some information on the x-coordinate will be lost when keeping a fixed number of projection images. This can be understood better from the following: if you have included in this tilt series of 31 images, the projection images from the structure tilted over -90 and $+90$ degrees, there is no information on the x-coordinate available in these 2 projection images, decreasing the total information on the x-coordinate from the whole tilt series as compared to a tilt series with the same number of projection images and a smaller tilt range. Based on the results of this analysis presented in Fig. 4, an angular tilt range of at least $[-70, 70]$ degrees can be suggested. This corresponds to the standard tilt range for conventional tomography experiments.

5.4. The optimal number of projection images

In this subsection, the lower bound on the standard deviation for locating the central atom of a nanocluster in 3D is evaluated as a function of the number of projections. In Fig. 5, the result is shown for a nanocluster with 309 atoms using a tilt range of $[-90, 90]$ degrees. The nanocluster was tilted in this range with a constant tilt increment for each number of projection images. An electron dose of 5555 $e^-/\text{Å}^2$ per image has been used for the tilt series of 31 images corresponding to the electron dose that has been used in the previous subsections. For the computation of the precision as a function of the number of projection images, the total incident electron dose has been kept constant, and the electron dose has been rescaled corresponding to the number of projection images. As expected, Fig. 5 shows that the precision improves when increasing the number of projection images. Beyond a certain value, the gain in precision is marginal. Therefore, more than 20 projection images can be suggested as an appropriate values.

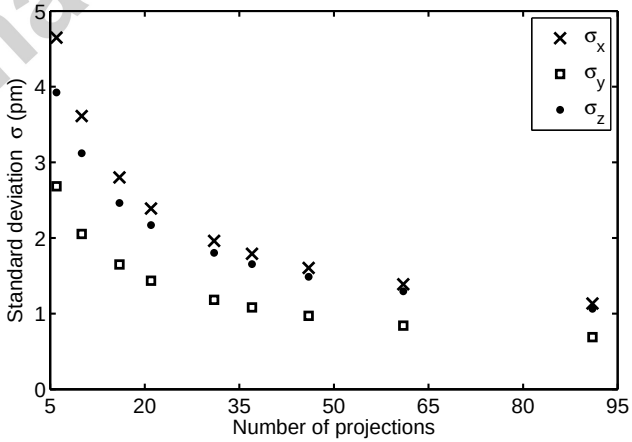

Figure 5: The precision σ of the x-, y-, and z-coordinate as a function of the number of projection images for locating the central atom of a nanocluster with 309 atoms based on simulations using the Gaussian approximation model with a tilt range of $[-90, 90]$ degrees and a fixed total electron dose.

5.5. The optimal detector range

Using the expression for the CRLB, the optimal experiment design for locating the central atom of a nanocluster in 3D can also be optimised in terms of the inner and outer angle of an annular STEM detector [34, 42–44]. In order to evaluate the precision as a function of the detector angles of the annular STEM detector, multislice simulations have been performed with varying detector angles. From the evaluation of the precision as a

function of the outer angle, it follows that the optimal outer detector radius should be as large as possible in the experiment. The inner angle has been varied between 15 mrad and 90 mrad. Figure 6 shows the precision as a function of the inner detector radius using the multislice simulations using 31 projection images, a tilt range of $[-90, 90]$ degrees and an electron dose of 5555 $e^-/\text{Å}^2$ per image. The optimal inner angle equals 21 mrad which equals the convergence angle used in the simulations. In this manner, dark field images can be acquired with the highest possible detected dose resulting in the highest attainable precision. It is important to note here that the experimental design for which the precision is optimal does not necessarily correspond to the experimental settings leading to the highest signal-to-noise ratio or the best image contrast. Here, the evaluation of the precision as a function of the inner detector radius suggests low angle annular dark field STEM imaging. Since in this imaging mode also coherent scattering contributes to the detected signal, this signal will be more sensitive for strain and defects. The here-presented analysis can also be applied to structures including defects and strain as this may have an influence on the choice of the proposed detector settings. Nevertheless, this result, where the optimal inner detector radius is equal to the convergence angle, gives a general guideline for the choice of the inner detector radius.

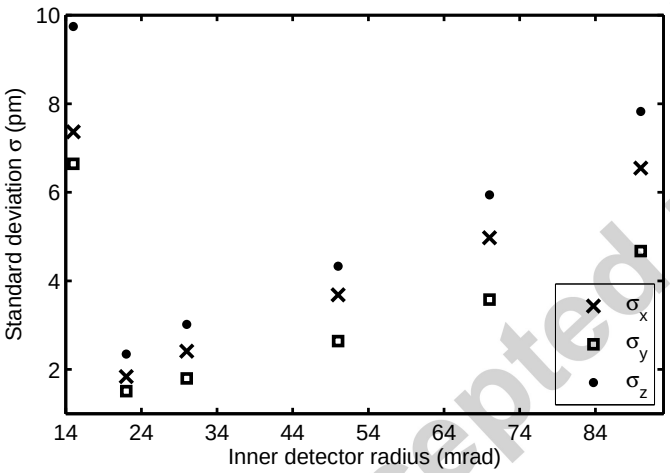

Figure 6: The precision σ of the x-, y-, and z-coordinate as a function of the inner detector radius for locating the central atom of a nanocluster with 309 atoms based on multislice simulations using 31 projection images, a tilt range of $[-90, 90]$ degrees and an incident electron dose of 5555 $e^-/\text{Å}^2$ per image.

5.6. The attainable precision for locating the central atom

In order to quantify the attainable precision for a set of realistic experimental settings, we used the suggested values obtained in the previous subsections, i.e. a tilt range of $[-72, 72]$ degrees, 25 projection images, an inner detector radius of 21 mrad, and an incident electron dose of 5555 $e^-/\text{Å}^2$ per image. For these settings, multislice simulations have been performed for the four gold nanoclusters. These simulations take into account the channelling effects. These channelling effects start to play an important role for the largest clusters and influence the derivatives which are needed for the calculation of the attainable precision. Therefore, using the multislice simulations the results for the attainable precision will be more realistic. In Fig. 7, the attainable precision of the x-, y-, and z-coordinate for locating the central atom of a nanocluster in 3D is shown for the experimental settings as a function of the cluster diameter for both the multislice simulations (MS) and the Gaussian approximation model (GM). From this figure, it is clear that the central atom of a small nanocluster can be located more precisely in 3D than the central atom of a larger nanocluster. Furthermore, it is shown that a precision of a few picometres is feasible in the presence of electron counting noise only. In addition, by comparing the values from the multislice simulations and the Gaussian approximation model, it can be concluded that the Gaussian approximation model is a reliable model for evaluating the attainable precision, since the calculated values for the attainable precision based on the Gaussian approximation model and the multislice method are very comparable. Experimentally, atomic resolution reconstructions have recently been obtained [11–15]. The precision with which the three-dimensional atom coordinates can be measured from these reconstruction is still an open question. In [15], it is mentioned that the three-dimensional coordinates of the atoms have been determined with a precision of ≈ 19 pm. Obviously, scan noise, alignment errors, the effect of a sample support, the rearrangement of surface atoms, and similar will significantly deteriorate the attainable precision, explaining the larger experimentally obtained precision. However, in this study, the purpose is to investigate the ultimate precision that can be attained. Therefore, it is assumed that scan noise and alignment errors can be avoided or can be corrected for in this analysis [16–18] and an ideal sample is assumed.

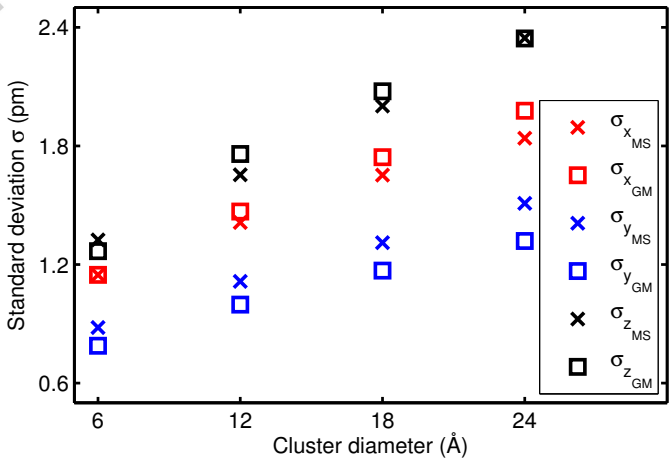

Figure 7: The attainable precision σ of the x-, y-, and z-coordinate as a function of the cluster diameter based on realistic multislice simulations (MS) and the Gaussian approximation model (GM) using the suggested experimental settings. A precision of w few picometres is feasible.

5.7. The precision as a function of the incident electron dose

The actual value of the precision does not only depend on the choice of the tilt range, the number of projection images, or the annular STEM detector range, but also on the incident electron

dose. In a STEM experiment the number of electrons per pixel is determined by Eq. (4). In Fig. 8, the precision of the x-, y-, and z-coordinate for locating the central atom of a nanocluster in 3D is shown as a function of the incident electron dose when using 25 projection images over a tilt range of $[-72, 72]$ degrees for a nanocluster of 309 atoms based on realistic multislice simulations. It is clear from this figure that, as one could expect, the precision increases, i.e. the standard deviation σ decreases, for an increasing electron dose. The precision is proportional to the incident electron dose as $\sqrt{N_e}$. If a precision of a few picometres is desired, then an electron dose of at least 10^3 e$^-$/Å^2 per image would be necessary. This evaluation can be of great importance if one wants to reduce beam damage but at the same time still obtain an acceptable precision to locate the atoms in 3D.

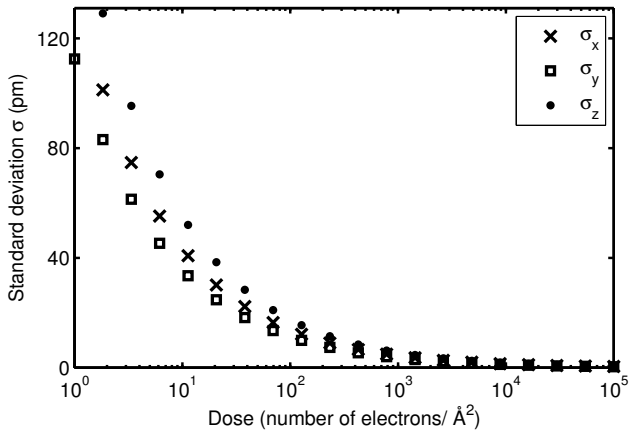

Figure 8: The precision σ of the x-, y-, and z-coordinate as a function of the dose per image (number of electrons/Å^2) for locating the central atom of a nanocluster with 309 atoms based on realistic multislice simulations with 25 projection images over a tilt range of $[-72, 72]$ degrees.

6. Conclusions

In this work, the theoretical limits with which the atoms of a nanocluster can be located in 3D based on the acquisition of a tilt series of ADF STEM images was investigated. Using the concept of the Cramér-Rao lower bound, a theoretical lower bound on the variance, quantitative measurements were obtained for the precision of the x-, y-, and z-coordinate when locating the central atom of a nanocluster in 3D. Furthermore, the here-described method is put forward as a powerful tool that can be used to optimise the design of an experiment. For this goal, the precision has been evaluated for locating the central atom of a gold cluster as a function of the incident electron dose, the angular tilt range, the number of projection images, the annular STEM detector range, and the cluster diameter. Obviously, the exact optimal experiment design and the exact values for the precision will depend on the material under study. Nevertheless, the conclusions from the study conducted in this paper give some general guidelines on optimal experiment design for extracting the location of the atoms in 3D using a tilt series of STEM images.

Using approximate STEM simulations, based on a Gaussian approximation model, the calculation of the precision was optimised, since this approach allows a full analytical computation of the precision. This reduces drastically the required number of simulations for the computation of the precision for accurate multislice simulations, where the precision is computed numerically. Using the Gaussian approximation model, suggestions for the angular tilt range and number of projection images could be obtained in an efficient and rapid manner. An angular tilt range of at least $[-70, 70]$ degrees and a minimal number of 20 projection images was found. In addition, it was shown that the precision for locating the central atom of a nanocluster is better for small nanoclusters. The optimisation of the detector angles requires multislice simulations. From this study, it could be concluded that an inner detector radius of the STEM detector equal to the convergence angle is optimal for locating the atoms of a nanocluster in 3D. Furthermore, simulations using the accurate multislice method are most appropriate for quantifying the ultimate precision that can be attained. In this paper, we demonstrated using accurate multislice simulations that a precision in the picometre range for locating the atoms in 3D is feasible in the presence of electron counting noise only, assuming ideal experimental conditions. In addition, the general framework presented in this paper to locate atoms in 3D from a tilt series of images can be applied to any structure of interest, such as more complex structures consisting of more than one atom type.

Acknowledgements

The authors acknowledge financial support from the European Union under the Seventh Framework Program under a contract for an Integrated Infrastructure Initiative. Reference No. 312483-ESTEEM2. The authors acknowledge financial support from the Research Foundation Flanders (FWO,Belgium) through project fundings (G.0374.13N, G.0369.15N and G.0368.15N), a post-doctoral grant to A. De Backer, and from the DFG under contract No. RO-2057/4-2.

Appendix A. The effect of the finite size of the source on the precision

In realistic STEM simulations, the finite size of the source is taken into account by a two-dimensional convolution with the intensity distribution of the source image. This intensity is often modelled as a Gaussian distribution with a FWHM of around 0.7 Å for an aberration corrected transmission electron microscope [29, 45]. However, it is known that the shape of the source image deviates significantly from a Gaussian profile [46, 47]. Measurements of the exact shape of the source size distribution show considerable longer tails as compared to a simple Gaussian profile. In order to study the effect of the shape of the source size distribution, the precision has been evaluated for 3 different values of the FWHM taken from Ref. [47]. The precision when using a simple Gaussian profile for taking into account source size broadening has been compared with

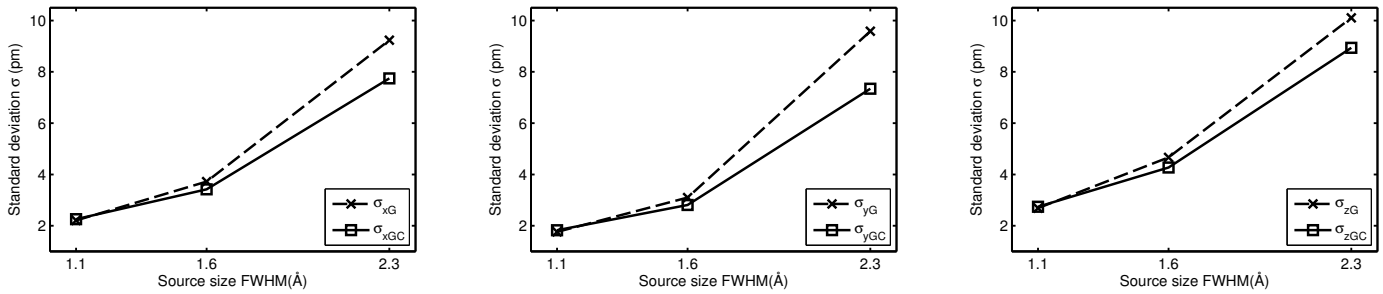

Figure A.9: The precision σ of the x-, y-, and z-coordinate (from left to right) as a function of FWHM of the source size profile for two different shapes of the source size for locating the central atom of a nanocluster with 13 atoms based on multislice simulations using 31 projection images, a tilt range of $[-90, 90]$ degrees, an inner detector radius of 21 mrad, and an incident electron dose of 5555 $e^-/\text{Å}^2$ per image. The subscripts G and GC refer to a simple Gaussian distribution and a linear combination of Gaussian and bivariate Lorentzian/Cauchy distribution, respectively, for the source size broadening profile.

the precision when using a linear combination of a Gaussian and a bivariate Lorentzian/Cauchy distribution. The precision for locating the central atom has been evaluated for a nanocluster of 13 atoms based on realistic multislice simulations using 31 projection images, a tilt range of $[-90, 90]$ degrees, an inner detector radius of 21 mrad, and an incident electron dose of 5555 $e^-/\text{Å}^2$ per image. As expected, Fig. A.9 shows that the precision improves when decreasing the FWHM of the source size. Moreover, this figure shows that when the FWHM of the source size is small that the Gaussian profile is a good approximation for taking into account source size broadening when computing the precision of the central atom of the nanocluster. The source size used in the paper has a FWHM of 0.7 Å. For this value, we expect that the difference between the two methods is negligible.

Appendix B. The effect of the Debye-Waller factor on the precision

In this section, it has been investigated if the assumption of the same Debye-Waller factor for all the atoms of a nanocluster is reasonable while evaluating the precision of the three-dimensional coordinates of the central atom of this nanocluster. For this purpose, the precision of this approach has been compared with the precision calculated based on multislice simulations using a different Debye-Waller factor for each atom. The smallest cluster has been chosen since for this cluster the effect would be the most pronounced. In order to obtain the Debye-Waller factors for each atom of the gold nanocluster with 13 atoms, molecular dynamic (MD) simulations were performed at $T = 300$ K. The simulation has been performed by using the LAMMPS software [48] and a potential calculated by G. Grochola has been used [49]. Using the root mean square atomic displacements obtained from this MD simulation, the following values for the Debye-Waller factor (Å^2) could be calculated, where the first value corresponds to the central atom and the other to the surface atoms of this cluster:

	0.59		→ central atom
3.10	3.82	3.91	
3.81	3.29	3.90	→ surface atoms
3.77	3.26	3.82	
3.81	3.92	3.03	

Next, the precision based on the multislice simulations with these different Debye-Waller factors for each atom has been calculated for the central atom of the cluster and compared with the precision obtained from the multislice simulations with the same Debye-Waller factor (DWF) of 0.63 Å^2:

	different DWF	same DWF
σ_x (pm)	1.1801	1.1399
σ_y (pm)	0.7925	0.7735
σ_z (pm)	1.0898	1.0633

From this values it can be concluded that the difference in precision is very small since the Debye-Waller factor of the central atom does not change a lot with respect to the value which is used when using the same Debye-Waller factor for all atoms of the nanocluster.

[1] J. A. Alonso, Structure and properties of atomic nanoclusters, Imperial College Press, 2005.

[2] G. B. Olson, Designing a new material world., Science 288 (2000) 993–998.

[3] Y. L. Tang, Y. L. Zhu, Y. J. Wang, W. Y. Wang, Y. B. Xu, W. J. Ren, Z. D. Zhang, X. L. Ma, Atomic-scale mapping of dipole frustration at 90° charged domain walls in ferroelectric $PbTiO_3$ films, Scientific Reports 4 (2014) 4115.

[4] N. Alem, O. V. Yazyev, C. Kisielowski, P. Denes, U. Dahmen, P. Hartel, M. Haider, M. Bischoff, B. Jiang, S. G. Louie, A. Zettl, Probing the Out-of-Plane Distortion of Single Point Defects in Atomic Thin Hexagonal Boron Nitride at the Picometer Scale, Physical Review Letters 106 (2011) 126102.

[5] T. Qi, I. Grinberg, A. M. Rappe, Correlations between tetragonality, polarization, and ionic dipslacement in $PbTiO_3$-derived ferroelectric perovskite solid solutions, Physical Review B 82 (2010) 134113.

[6] P. A. Midgley, M. Weyland, 3D electron microscopy in the physical sciences: the development of Z-contrast and EFTEM tomography, Ultramicroscopy 96 (2003) 413–431.

[7] P. A. Midgley, R. E. Dunin-Borkowski, Electron tomography and holography in materials science, Nature Materials 8 (2009) 271–280.

[8] S. Bals, S. Van Aert, G. Van Tendeloo, High resolution electron tomography, Current Opinion in Solid State and Materials Science 17 (2013) 107–114.

[9] N. Tanaka, Scanning Transmission Electron Microscopy of Nanomaterials: Basics of Imaging and Analysis, Imperial College Press, 2014.

[10] S. J. Pennycook, P. D. Nellist, Scanning Transmission Electron Microscopy Imaging and Analysis, Springer, 2011.

[11] S. Van Aert, K. J. Batenburg, M. D. Rossell, R. Erni, G. Van Tendeloo, Three-dimensional atomic imaging of crystalline nanoparticles, Nature 470 (2011) 374–377.

[12] S. Bals, M. Casavola, M. A. van Huis, S. Van Aert, K. J. Batenburg, G. Van Tendeloo, D. Vanmaekelbergh, Three-Dimensional Atomic Imaging of Colloidal Core-Shell Nanocrystals, Nano Letters 11 (8) (2011) 3420–3424.

[13] B. Goris, S. Bals, W. Van den Broek, E. Carbo-Argibay, S. Gomez-Grana, L. M. Liz-Marzan, G. Van Tendeloo, Atomic-scale determination of surface facets in gold nanorods, Nature Materials 11 (2012) 930–935.

[14] B. Goris, J. De Beenhouwer, A. De Backer, D. Zanaga, K. J. Batenburg, A. Sánchez-Iglesias, L. M. Liz-Marzán, S. Van Aert, S. Bals, J. Sijbers, G. Van Tendeloo, Measuring Lattice Strain in Three Dimensions through Electron Microscopy, Nano Letters 15 (10) (2015) 6996–7001.

[15] R. Xu, C.-C. Chen, L. Wu, M. C. Scott, W. Theis, C. Ophus, M. Bartels, Y. Yang, H. Ramezani-Dakhel, M. R. Sawaya, H. Heinz, L. D. Marks, P. Ercius, J. Miao, Three-dimensional coordinates of individual atoms in materials revealed by electron tomography, Nature Materials 14 (2015) 1099–1103.

[16] L. Jones, P. D. Nellist, Identifying and Correcting Scan Noise and Drift in the Scanning Transmission Electron Microscope, Microscopy and Microanalysis 19 (2013) 1050–1060.

[17] A. B. Yankovich, B. Berkels, W. Dahmen, P. Binev, S. I. Sanchez, S. A. Bradley, A. Li, I. Szlufarska, Voy, Picometre-precision analysis of scanning transmission electron microscopy images of platinum nanocatalysts, Nature Communications 5 (2014) 4155.

[18] L. Jones, H. Yang, T. J. Pennycook, S. J. Marshall, S. Van Aert, N. D. Browning, M. R. Castell, P. D. Nellist, Smart Align - a new tool for robust non-rigid registration of scanning microscope data, Advanced Structural and Chemical Imaging.

[19] L. Rayleigh, Xxxi. Investigations in optics, with special reference to the spectroscope, Philosophical Magazine Series 5 8 (49) (1879) 261–274.

[20] E. Bettens, D. Van Dyck, A. J. den Dekker, J. Sijbers, A. van den Bos, Model-based two-object resolution from observations having counting statistics, Ultramicroscopy 77 (1999) 37–48.

[21] S. Van Aert, A. J. den Dekker, D. Van Dyck, A. van den Bos, High-resolution electron microscopy and electron tomography: resolution versus precision, Journal of Structural Biology 138 (2002) 21–33.

[22] B. C. Curley, R. L. Johnston, N. P. Young, Z. Y. Li, M. Di Vece, R. E. Palmer, A. Bleloch, Combining Theory and Experiment to Characterize the AtomicStructures of Surface-Deposited Au_{309} Clusters, Journal of Physical Chemistry C 111 (2007) 17846–17851.

[23] J. M. Cowley, A. F. Moodie, The scattering of electrons by atoms and crystals. I. A new theoretical approach, Acta Crystallographica 10 (10) (1957) 609–619.

[24] K. Ishizuka, A practical approach for STEM image simulation based on the FFT multislice method, Ultramicroscopy 90 (2002) 71–83.

[25] P. Rez, The use of array processors attached to minicomputers for multislice image calculations, Ultramicroscopy 16 (1985) 255–260.

[26] E. J. Kirkland, Advanced Computing in Electron Microscopy, 2nd Edition, Springer, 2010.

[27] E. J. Kirkland, R. F. Loane, J. Silcox, Simulation of annular dark field STEM images using a modified multislice method, Ultramicroscopy 23 (1987) 77–96.

[28] L. J. Allen, S. D. Findlay, M. P. Oxley, C. J. Rossouw, Lattice-resolution contrast from a focus coherent electron probe. Part I, Ultramicroscopy 96 (2003) 47–63.

[29] J. M. LeBeau, S. D. Findlay, L. J. Allen, S. Stemmer, Quantitative Atomic Resolution Scanning Transmission Electron Microscopy, Physical Review Letters 100 (2008) 206101.

[30] A. Rosenauer, K. Gries, K. Müller, A. Pretorius, M. Schowalter, A. Avramescu, K. Engl, S. Lutgen, Measurement of specimen thickness and composition in $Al_xGa_{1-x}N$/GaN using high-angle annular dark field images, Ultramicroscopy 109 (2009) 1171–1182.

[31] A. Rosenauer, M. Schowalter, Stemsim - a new software tool for simulation of STEM HAADF Z-contrast imaging, in: A. Cullis, P. Midgley (Eds.), Microscopy of Semiconducting Materials 2007, Vol. 120 of Springer Proceedings in Physics, Springer Netherlands, 2008, pp. 170–172.

[32] C. Mory, M. Tence, C. Colliex, Theoretical-Study Of The Characteristics Of The Probe For A Stem With A Field-Emission Gun, Journal De Microscopie Et De Spectroscopie Electroniques 10 (5) (1985) 381–387.

[33] A. J. Logsdail, Computational Characterisation of Gold Nanocluster Structures, Springer International Publishing Switzerland, 2013.

[34] S. Van Aert, A. J. den Dekker, D. Van Dyck, A. van den Bos, Optimal experimental design of STEM measurement of atom column positions, Ultramicroscopy 90 (4) (2002) 273 – 289.

[35] A. van den Bos, Parameter estimation for scientists and engineers, Wiley, 2007.

[36] A. van den Bos, A. J. den Dekker, Resolution reconsidered - conventional approaches and an alternative, Advances in Imaging and Electron Physics 117 (2001) 241–360, san Diego: Academic Press.

[37] A. M. Mood, F. A. Graybill, D. C. Boes, Introduction to the Theory of Statistics (1974).

[38] M. G. Kendall, A. Stuart, The Advanced Theory of Statistics: In three volumes. Volume 2. Inference and Relationship (1967).

[39] A. L. Mackay, A dense non-crystallographic packing of equal spheres, Acta Crystallographica 15 (9) (1962) 916–918.

[40] O. Scherzer, The Theoretical Resolution Limit of the Electron Microscope, Journal of Applied Physics 20 (1949) 20–29.

[41] M. Weyland, D. A. Muller, Tuning the convergence angle for optimum STEM performance, FEI nanoSolutions 1 (2005) 24–35.

[42] J. Gonnissen, A. De Backer, A. J. den Dekker, G. T. Martinez, A. Rosenauer, J. Sijbers, S. Van Aert, Optimal experimental design for the detection of light atoms from high-resolution scanning transmission electron microscopy images, Applied Physics Letters 105 (2014) 063116.

[43] A. De Backer, A. De wael, J. Gonnissen, S. Van Aert, Optimal experimental design for nano-particle atom-counting from high-resolution stem images, Ultramicroscopy 151 (2015) 46–55.

[44] J. Gonnissen, A. De Backer, A. J. den Dekker, S. Van Aert, Detecting and locating light atoms from high-resolution stem images: The quest for a single optimal design, Ultramicroscopy-Doi:10.1016/j.ultramic.2016.07.014.

[45] C. Dwyer, R. Erni, J. Etheridge, Method to measure spatial coherence of subangstrom electron beams, Applied Physics Letters 93 (2008) 021115.

[46] C. Dwyer, R. Erni, J. Etheridge, Measurement of effeffect source distribution and its importance for quantitative interpretation of STEM images, Ultramicroscopy 110 (2010) 952–957.

[47] J. Verbeeck, A. Bch, W. Van den Broek, A holographic method to measure source size broadening in STEM, Ultramicroscopy 120 (2012) 35–40.

[48] S. Plimpton, Fast parallel algorithms for short-range molecular dynamics, Journal of computational physics 117 (1) (1995) 1–19.

[49] G. Grochola, S. P. Russo, I. K. Snook, On fitting a gold embedded atom method potential using the force matching method, The Journal of chemical physics 123 (20) (2005) 204719.